New Journal of Physics
The open access journal at the forefront of physics

Deutsche Physikalische Gesellschaft DPG
IOP Institute of Physics

Published in partnership with: Deutsche Physikalische Gesellschaft and the Institute of Physics

OPEN ACCESS

RECEIVED
12 February 2018

REVISED
12 April 2018

ACCEPTED FOR PUBLICATION
27 April 2018

PUBLISHED
15 May 2018

PAPER

Einstein–Bose condensation of Onsager vortices

Rahil N Valani[1,2], **Andrew J Groszek**[1] **and Tapio P Simula**[1]

[1] School of Physics and Astronomy, Monash University, Victoria 3800, Australia
[2] Department of Mechanical and Aerospace Engineering, Monash University, Victoria 3800, Australia

E-mail: tapio.simula@monash.edu

Keywords: Onsager vortex, quantum turbulence, superfluidity, absolute negative temperature, quantised vortices, vortex–particle duality, Bose–Einstein condensation

Abstract

We have studied statistical mechanics of a gas of vortices in two dimensions. We introduce a new observable—a condensate fraction of Onsager vortices—to quantify the emergence of the vortex condensate. The condensation of Onsager vortices is most transparently observed in a single vortex species system and occurs due to a competition between solid body rotation (see vortex lattice) and potential flow (see multiple quantum vortex state). We propose an experiment to observe the condensation transition of the vortices in such a single vortex species system.

1. Introduction

Perhaps the most astonishing aspect of turbulence is not the complexity of its dynamics but rather that it feeds the emergence of ordered structures out of chaos. The ubiquity of large eddies in two-dimensional (2D) fluid flows was also noted by Onsager who suggested that it might be possible to obtain a statistical mechanics description of hydrodynamic turbulence of 2D flows based on discrete collections of point-like vortex particles [1]. In particular, Onsager predicted that turbulent 2D systems could support large scale clustered vortex structures, later coined Onsager vortices, and that such structures would correspond to negative absolute temperature states of the vortex degrees of freedom [2]. Notwithstanding the negative absolute Boltzmann temperature states were observed in nuclear spin systems [3–5] soon after Onsager's theoretical prediction, and more recently in the motional degrees of freedom of cold atoms confined in optical lattices [6], the negative temperature Onsager vortex states in their original context of 2D (super)fluid turbulence have remained elusive, until recently. Indeed, the first experimental observations of negative absolute temperature Onsager vortex states in Bose–Einstein condensates have been reported [7, 8]. The most extreme negative temperature attained in these experiments was estimated to be $T = 1.14\,T_c$, where T_c denotes the critical temperature at which the Onsager vortices first form a condensate. We anticipate that further developments may enable vortex states with even higher energy to be created and the crossing of the critical temperature to be observed.

Kraichnan developed Onsager's ideas on 2D turbulence further, conjecturing that a scale invariant inverse energy cascade mechanism of incompressible kinetic energy could dynamically lead to the formation of Onsager vortices and even to their condensation and that: *'The phenomenon is analogous to the Einstein–Bose condensation of a finite 2D quantum gas'* [9]. In the Kraichnan model the system scale Onsager vortex clusters would emerge due to a termination of the inverse cascade that accumulates energy at ever larger spatial scales. Ultimately, such a process could potentially lead to the condensation of the Onsager vortices, which correspond to the highest accessible energy states of the vortex degrees of freedom [9, 10]. In a neutral system with $N_{\rm tot}$ vortices in total, the condensation of Onsager vortices occurs at a critical negative temperature $T_{\rm EBC} = -\alpha N_{\rm tot}/4$ [11–13], where $\alpha = \rho_s\kappa^2/4\pi k_{\rm B} = T_{\rm HH}$ is the critical positive temperature for the Hauge–Hemmer pair-collapse transition [14, 15], which in the case of non-zero vortex core size becomes renormalised to the Berezinskii–Kosterlitz–Thouless (BKT) critical temperature $T_{\rm BKT} = T_{\rm HH}/2$ [16–18]. Here $k_{\rm B}$ is the Boltzmann constant, ρ_s is the (super)fluid density and $\kappa = h/m$ is the circulation quantum with h the Planck's constant and m the particle mass. Inspired by Kraichnan's insight [9, 10], we refer to the critical temperature of condensation of Onsager

vortices with the acronym EBC, which stands for Einstein–Bose condensation, and in the case of zero-core point vortices is also known as supercondensation [10].

The recent developments of imaging and manipulating compressible superfluids have sparked renewed interest in Onsager's statistical hydrodynamics theory of turbulence. Experiments employing harmonically trapped Bose–Einstein condensates of atoms have ranged from studies of dynamics of vortex dipoles [19] or few vortices [20] to three- [21] and 2D [22–25] quantum turbulence. Moreover, uniform atom traps are becoming increasingly popular [7, 8, 26–33] and will be particularly useful for studies of quantum turbulence. This is partly because well defined trap walls enhance the vortex clustering signal in comparison to harmonically trapped systems [13, 23, 34, 35]. In the latter case, strong clustering has not been observed although in both cases Onsager vortices in decaying 2D quantum turbulence has been predicted to emerge via an evaporative heating mechanism of vortices [13, 34].

The successes of the recent experimental developments have also spawned novel theoretical investigations [13, 34–45]. In addition to visual inspection, the presence of Onsager vortices has been associated with indicators such as the vortex dipole moment [13, 34], vortex clustering measures [7, 8, 36, 37, 40], or a peak in the power spectral density of incompressible kinetic energy [8, 13, 38, 46]. However, a measurable that would quantify the degree of condensation of the vortices as opposed to their clustering, has been lacking. Here we use *a vortex–particle duality* to define a condensate fraction that enables quantitative measurements of condensation of Onsager vortices in these 2D systems [47]. We have implemented a vortex classification algorithm based on the prescription by Reeves *et al* [37], which can be used as a quantitative measure of vortex clustering. Together with the condensate fraction measurable introduced here that uniquely identifies the condensate of Onsager vortices, these two observables enable acquisition of detailed information on clustering and condensation of vortices. We find that the condensate fraction exhibits universal behaviour independent of the number of vortices in the bounded circular system. In contrast to condensation, clustering of vortices is present at all negative temperatures in the sense that the total number of vortices belonging to vortex clusters of varying size is greater than zero [45]. Vortex clustering is a precursor to the condensation of Onsager vortices and is reminiscent of the quasi-condensation that precedes the superfluid phase transitions in low-dimensional quantum gas systems [48–51].

2. Vortex–particle duality

It is not possible to localise the position of a real vortex inside an area smaller than the vortex core. Consequently, any zero-core point vortex model with $\xi = 0$ violates Heisenberg uncertainty principle and fails to correctly describe the physics of the condensate of Onsager vortices. It is therefore paramount to introduce a non-vanishing vortex core size to the point vortex model in order to describe physics of the low entropy negative temperature states with $T/T_{\rm EBC} < 1$. Hence, to avoid the unphysical consequences in the high energy states of the point vortex model, from this point on and unless otherwise stated, we will replace the point vortices with hard core vortices. In practice, this can be implemented by constraining the Hamiltonian, equation (1), by not allowing the centres of any two vortices to be located closer than one vortex core diameter from each other.

We first consider $N_{\rm tot}$ singly quantised point-like vortices with a hard core of radius ξ and equal numbers of clockwise and counter-clockwise circulations confined in a circular disc of radius $R_\circ$, unless stated otherwise. The pseudo-Hamiltonian describing our system is [13, 52]:

$$H = \alpha k_{\rm B} \sum_j s_j^2 \ln(1 - r_j^2) - \alpha k_{\rm B} \sum_{i<j} s_i s_j \ln(r_{ij}^2) + \alpha k_{\rm B} \sum_{i<j} s_i s_j \ln(1 - 2x_i x_j - 2y_i y_j + r_i^2 r_j^2), \tag{1}$$

where $r_j^2 = x_j^2 + y_j^2$ and x_j and y_j are the dimensionless Cartesian coordinates of the jth vortex measured in units of the system radius $R_\circ$ and $s_j = \pm 1$ determines the circulation direction of the jth vortex. The first, single vortex, logarithmic term is due to the interaction of each vortex with its own image, the second represents the pairwise 2D Coulomb-like interaction between ith and jth vortex separated by distance r_{ij} and the last term, due to the circular boundary, represents the interaction of system vortices with the images of all other vortices.

The dynamics of the point-like vortices are determined by the equations of motion [1]

$$hs_j \frac{\partial x_j}{\partial t} = \frac{\partial H}{\partial y_j} \quad \text{and} \quad hs_j \frac{\partial y_j}{\partial t} = -\frac{\partial H}{\partial x_j}. \tag{2}$$

To draw a closer correspondence with Hamiltonian mechanics, we may assign for each vortex a canonical coordinate $q_j = R_\circ x_j$ and momentum $p_j = -m_v \omega_0 R_\circ y_j$, where m_v is the vortex mass [53] and ω_0 is an angular frequency. Thus the set of vortex coordinates $\{x_j, y_j\}$ in the real space are mapped onto points in the phase space

$\{q_j, p_j\}$ spanned by the canonical conjugate variables. In this Hamiltonian description the vortex particles move in one-dimensional (1D) real space tracing out orbits in the 2D phase space, which is bounded by the circular wall of radius R_o. Equation (2) establishes the *vortex–particle duality*—that a vortex in a 2D fluid may behave as a particle in a 1D space.

Motivated by the vortex–particle duality and in contrast to Kraichnan's conjecture, we anticipate the condensation of Onsager vortices to be analogous to the condensation of a finite 1D quantum gas. Interestingly, in the 2D fluid picture the vortex condensate corresponds to maximum kinetic energy states of the fluid whereas in the 1D dual picture the condensate corresponds to zero momentum state of the 1D vortex particles.

3. Ideal vortex gas approximation

By ignoring the vortex–vortex interactions we obtain an ideal-gas model of vortex particles. A Maclaurin series expansion of the single vortex term in equation (1) with respect to r_j formally yields a 1D harmonic oscillator Hamiltonian

$$H_0 = \alpha k_B \sum_j s_j^2 \ln(1 - r_j^2) \approx -\sum_j \left(\frac{p_j^2}{2m_v} + \frac{1}{2} m_v \omega_0^2 q_j^2 \right), \tag{3}$$

where the oscillator frequency is defined as $\omega_0 \equiv \sqrt{\frac{k}{m_v}}$ in terms of the elastic constant $k = \frac{\rho_s \kappa^2}{2\pi R_o^2}$, with an inverted energy spectrum with respect to the canonical case. Within the harmonic approximation, a single vortex ν of this system will travel along a periodic phase space orbit $\{q_\nu, p_\nu\} = \{R_\nu \cos(\omega_\nu t), -m_\nu \omega_0 R_\nu \sin(\omega_\nu t)\}$, with orbital angular frequency ω_ν and semi-axis R_ν.

The Einstein–Brillouin–Keller semiclassical quantisation rule [54]

$$\oint p_\nu \, dq_\nu = \left(n + \frac{k}{4} \right) h, \tag{4}$$

where n is the principal quantum number and k is the Keller–Maslov index then evaluates to

$$\int_0^T p_\nu \, dq_\nu = \int_0^{\frac{2\pi}{\omega_\nu}} \omega_\nu m_\nu \omega_0 R_\nu^2 \sin^2(\omega_\nu t) \, dt = \pi m_\nu \omega_0 R_\nu^2, \tag{5}$$

where we have integrated over one period, $T = 2\pi/\omega_\nu$, of the vortex orbit. The 1D oscillatory motion has two classical turning points, $k = 2$, and therefore the quantisation rule, the combination of equations (4) and (5), yields the energy spectrum $E_n = (n + \frac{1}{2})\hbar\omega_0 = \frac{1}{2} m_\nu \omega_0^2 R_\nu^2$. This implies a minimum semi-axis $\min(R_\nu) = \xi$ for the vortex trajectories and yields the zero-point energy $E_0 = \frac{1}{2} m_\nu \omega_0^2 \xi^2$. In correspondence with the Heisenberg uncertainly relation, $\Delta q \Delta p \gtrsim \hbar/2$, the zero-point energy carries the information that the area of the phase space is quantised in units of $\hbar = m_\nu \omega_0 \xi^2$. This reflects the stated fact that it is not possible to localise the position of the vortex inside an area smaller than the vortex core.

4. Interacting vortex gas approximation

The velocity field induced by the vortices mediates strong vortex–vortex interactions such that the ideal-vortex approximation is strictly only valid for one vortex near the centre of the disk. However, the second term in equation (1) may be approximated as a mean-field potential by integrating out the spatial scales smaller than the intervortex spacing.

A neutral superfluid that locally rotates at an orbital angular frequency Ω with N_ν vortices of the same sign mimics the rotation of a classical fluid by having an areal vortex density

$$n_\nu = \frac{N_\nu}{\pi R^2} = \frac{m\Omega}{\pi\hbar}. \tag{6}$$

Hence, the mean superfluid velocity is $v(r) = \Omega r$, where r is the distance measured from the centre of such a rotating cluster of vortices with radius R. In contrast, in a high-winding number vortex with N_ν circulation quanta, the superfluid velocity field $v(r) = \frac{\hbar}{m} \frac{N_\nu}{r}$ is a gradient of a scalar phase function. In general, the velocity field is therefore

$$v(r) = N_\nu \frac{\hbar}{m} \frac{r}{(R^*)^2}; \quad r < R^*, \tag{7}$$

$$v(r) = N_\nu \frac{\hbar}{m} \frac{1}{r}; \quad r > R^*, \tag{8}$$

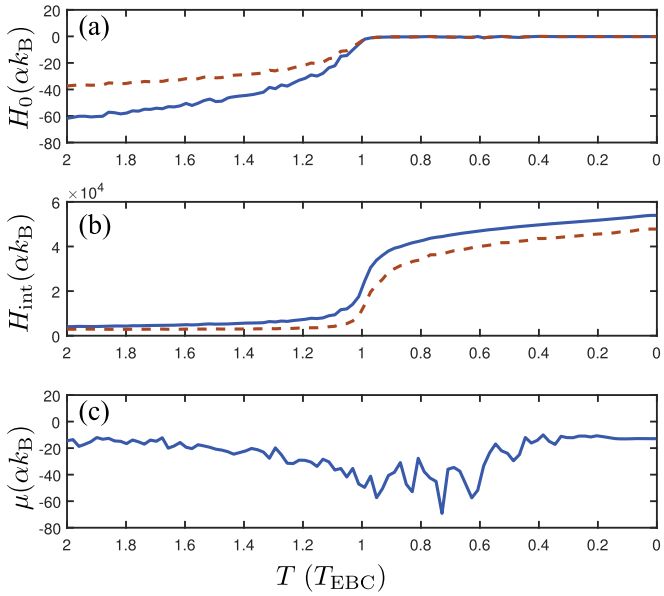

Figure 1. The three energy terms (a)–(c) of equation (1), solid lines, and the respective approximations equations (3) and (9), dashed lines, as functions of reduced temperature for $N_v = 100$ single species, $s = +1$, vortices. The large statistical fluctuations evident in (c) arise due to stray vortices that escape the central vortex cluster and approach their image vortices closer to the boundaries of the system. However, the magnitude of these fluctuations is insignificant in comparison to the energy scale in (b).

which is a combination of solid body rotation for $r < R^*$ and potential flow for $r > R^*$, where R^* is the radius of the vortex cluster. The kinetic energy associated with such a flow field may therefore be approximated by a mean-field interaction

$$\begin{aligned} H_{\rm int} &= -\alpha k_{\rm B} \sum_{i<j} s_i s_j \ln(r_{ij}^2) \\ &\approx \int_0^{2\pi} \int_0^{R_\circ} \frac{1}{2}\rho_s v^2(r)\, r\, {\rm d}r{\rm d}\theta \\ &= \pi \rho_s N_v^2 \frac{\hbar^2}{m^2}\left(\frac{1}{4} + \ln\left(\frac{R_\circ}{R^*}\right)\right). \end{aligned} \tag{9}$$

The final term in the Hamiltonian, equation (1), describes the remaining interaction with image vortices and yields an energy shift

$$-\mu = \alpha k_{\rm B} \sum_{i<j} s_i s_j \ln(1 - 2x_i x_j - 2y_i y_j + r_i^2 r_j^2). \tag{10}$$

Combining equations (3), (9), and (10), we thus arrive at the effective 1D vortex–particle Hamiltonian,

$$H_{\rm eff} = H_0 + H_{\rm int} - \mu \approx -\sum_{j=1}^{N_v}\left(\frac{p_j^2}{2m_v} + \frac{1}{2}m_v\omega_0^2 q_j^2\right) + \frac{\rho_s \kappa^2}{4\pi} N_v^2\left[\frac{1}{4} + \ln\left(\frac{R_\circ}{R^*}\right)\right] - \mu \tag{11}$$

that describes a system of 1D strongly interacting harmonic oscillators. It may be worth pointing out that the two forms in equation (9) have quite different interpretations. The first line is a *long-range interaction* of the vortices in 2D, whereas the last line is a strong *contact interaction* between 1D vortex particles with a coupling strength that is running with the energy scale set by the radius R^* of the cluster. In the Tonks–Girardeau-like limit of $R^* \to 0$ the effective coupling constant $g_{\rm 1} \propto \ln\left(\frac{R_\circ}{R^*}\right) \to \infty$ and equation (11) reduces to a semi-classical version of the Lieb–Liniger model [55].

Figure 1 shows the independent contributions of the three terms in the Hamiltonian, equation (1), for a system of 100 like-signed vortices as functions of reduced temperature. The details of this calculation are described in section 8. For comparison, the energy contributions due to the harmonic oscillator and mean-field approximations, equations (3) and (9), respectively, are shown by dashed lines. The harmonic oscillator approximation, equation (3), is better at lower reduced temperatures because the vortices clump close to the centre of the disk. However, since the mean-field term, equation (9), is proportional to N_v^2, it is overwhelmingly larger than the single vortex terms, which are proportional to N_v. These results establish that the mean-field Hamiltonian equation (11) is a reasonable approximation for equation (1) in this system.

5. Fraction of condensed vortices

On the basis of the vortex–particle duality, we anticipate condensation of Onsager vortices when the phase space density $n_v\lambda_v \gtrsim 1$. Here n_v is the 1D mean vortex density and

$$\lambda_v = \frac{h}{\langle p \rangle} \sim \frac{2\pi\xi^2}{\langle R_v \rangle} \tag{12}$$

is the thermal vortex de-Broglie wavelength, which in the vortex dual is inversely proportional to the size of an average temperature-dependent vortex orbit in the phase space. For N^* vortices confined within length $2R^*$ the condensation criterion becomes $\pi N^*\xi^2/\langle R_v \rangle R^* \sim 1$, which shows that condensation is expected when the vortices concentrate into a phase-space cluster with size of the order of $\xi\sqrt{N^*}$.

These considerations lead us to define the fraction of condensed vortices as the ratio, N_0/N, of N_0 vortices of a given sign in a single many-vortex cluster to the total number of vortices N of that same sign in the system. The highest density of vortices is found within clusters and by denoting N^* to be the number of vortices in the largest cluster, which will be the first to condense, and $A^0 = N^*\hbar = N^* m_v \omega_0 \xi^2$ and $A^* = N^* m_v \omega_0 \langle r_{\rm nn} \rangle^2$ to be, respectively, the minimum possible phase space area occupied by the N^* vortices and the phase space area actually covered by them, we obtain

$$\frac{N_0}{N} = \frac{N^*}{N}\frac{A^0}{A^*} = \frac{N^*}{N}\frac{\xi^2}{\langle r_{\rm nn} \rangle^2}. \tag{13}$$

Thus the condensate fraction is the product of the largest cluster fraction N^*/N and the square of the ratio of single vortex core radius ξ to the mean radius $\langle r_{\rm nn} \rangle$ of the effective area occupied by a vortex within the cluster, where $r_{\rm nn}$ is one half of the distance between the centres of nearest neighbour vortices in such a cluster. Although for single vortex species systems $N^*/N = 1$, in general, the system contains both vortices and antivortices and to measure $N^* < N$ in such systems, clusters of like-signed vortices must first be identified by a vortex classification algorithm.

6. Vortex classification algorithm

To quantitatively study clustering and condensation of vortices we have implemented a vortex classification algorithm based on the prescription by Reeves *et al* [37]. We assign each vortex in a given configuration of N vortices a unique and arbitrarily chosen label from the set $\{\nu_1, \nu_2, \ldots, \nu_N\}$. The vortex configuration is then described by a corresponding set of positions $\{z_1, z_2, \ldots, z_N\}$ (in 2D complex co-ordinates, where $z_j = x_j + iy_j$) and circulation signs $\{s_1, s_2, \ldots, s_N\}$, which here take the value $s_j = \pm 1$, denoting clockwise or anti-clockwise circulation. The algorithm does not prioritise any vortex and yields the same classification outcome regardless of the choice of vortex labelling. Figure 2 shows an example configuration of twelve judiciously numbered point vortices. The vortex classification algorithm is outlined below.

6.1. Step 1: Find dipole and cluster candidates

For each vortex ν_j, we locate the nearest opposite sign (NOS) vortex and label it as $(\nu_{\rm NOS})_j$ (i.e. the nearest vortex which satisfies $s_j (s_{\rm NOS})_j < 0$). We define the distance to this vortex to be $(R_{\rm NOS})_j \equiv |z_j - (z_{\rm NOS})_j|$. We then check to see if any other vortices (which are same-sign, by necessity) fall within the disk of radius $R_{\rm NOS}$ centred at vortex ν_j.

(i) *Dipoles:* If not, then $(\nu_{\rm NOS})_j$ is labelled as a dipole candidate for ν_j (e.g. in figure 2(a), ν_2 is labelled as a dipole candidate for ν_1).

(ii) *Clusters:* If there are $n_j \geqslant 1$ vortices which are nearer to ν_j than $(\nu_{\rm NOS})_j$, then these are labelled as cluster candidates for ν_j (e.g. vortex ν_{10} in figure 2(a), for which ν_9, ν_{11} and ν_{12} are cluster candidates).

Each vortex ν_j now has a corresponding set of candidate vortex labels, which we denote by $\boldsymbol{l}_j$. For case (i), $\boldsymbol{l}_j$ consists of a single opposite sign vortex, which is a dipole candidate. For case (ii), $\boldsymbol{l}_j$ is a list of n_j same-sign cluster candidates.

Table 1 below displays the lists $\boldsymbol{l}_j$ that are constructed in Step 1 of the algorithm when it is applied to the configuration shown in figure 2.

6.2. Step 2: Find mutually agreeing candidates

In the second step of the algorithm, the lists $\boldsymbol{l}_j$ are checked sequentially for mutual members. This process is shown schematically in figure 3 for the example configuration shown in figure 2 and table 1.

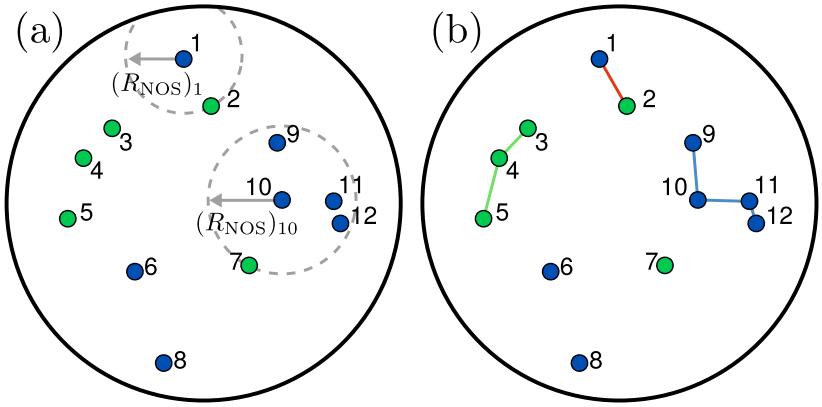

Figure 2. A configuration of twelve point vortices, (a) before and (b) after the classification algorithm has been applied. Vortices are drawn in blue, while antivortices are drawn in green. In panel (a), dashed circles are drawn centred on v_1 and v_{10}, denoting the respective distances $(R_{\rm NOS})_j$ to the nearest opposite signed vortex. Because v_2 is the closest vortex to v_1 and is of opposite sign, v_2 is labelled as a dipole candidate for v_1. Vortex v_{10}, on the other hand, is closer to v_9, v_{11} and v_{12} than it is to v_7; hence, these three vortices become cluster candidates for v_{10}. The lines joining clustered vortices in (b) are drawn using a minimum spanning tree algorithm, which is applied once all vortices have been labelled into the sets of clusters, dipoles or free vortices.

Table 1. Collation of $\boldsymbol{l}_j$ lists for the configuration shown in figure 2 after dipole and cluster candidates have been identified. Each row corresponds to a particular vortex v_j (leftmost column) and the list of all other vortices, ordered from left to right in increasing distance from v_j. Vortices/antivortices v_k are denoted with blue/green font if $|z_j - z_k| \leqslant (R_{\rm NOS})_j$. All vortices for which $|z_j - z_k| > (R_{\rm NOS})_j$ are coloured in grey, as these cannot be dipole or cluster candidates. The lists $\boldsymbol{l}_j$ consist of either a single opposite sign vortex (e.g. row 1, corresponding to vortex v_1, which has $\boldsymbol{l}_1 = \{v_2\}$), or a set of $\geqslant$1 same-sign vortices (e.g. row 4, corresponding to vortex v_4, for which $\boldsymbol{l}_4 = \{v_3, v_5\}$).

v_j	$\boldsymbol{l}_j$										
v_1	v_2	v_3	v_9	v_4	v_{10}	v_5	v_{11}	v_7	v_6	v_{12}	v_8
v_2	v_1	v_9	v_3	v_{10}	v_4	v_{11}	v_7	v_{12}	v_5	v_6	v_8
v_3	v_4	v_1	v_2	v_5	v_6	v_9	v_{10}	v_7	v_{11}	v_8	v_{12}
v_4	v_3	v_5	v_6	v_2	v_1	v_9	v_7	v_{10}	v_8	v_{11}	v_{12}
v_5	v_4	v_6	v_3	v_8	v_2	v_7	v_1	v_{10}	v_9	v_{11}	v_{12}
v_6	v_5	v_8	v_7	v_4	v_3	v_{10}	v_2	v_9	v_{12}	v_{11}	v_1
v_7	v_{10}	v_{12}	v_{11}	v_6	v_9	v_8	v_2	v_5	v_3	v_4	v_1
v_8	v_6	v_7	v_5	v_{10}	v_4	v_{12}	v_{11}	v_3	v_9	v_2	v_1
v_9	v_{10}	v_2	v_{11}	v_{12}	v_7	v_1	v_3	v_4	v_6	v_5	v_8
v_{10}	v_{11}	v_9	v_{12}	v_7	v_2	v_6	v_1	v_3	v_8	v_4	v_5
v_{11}	v_{12}	v_{10}	v_9	v_7	v_2	v_1	v_6	v_3	v_8	v_4	v_5
v_{12}	v_{11}	v_{10}	v_7	v_9	v_2	v_6	v_8	v_1	v_3	v_4	v_5

(i) *Dipoles:* If a list $\boldsymbol{l}_j$ consists of a single dipole candidate v_k, then the list $\boldsymbol{l}_k$ is checked to see if it contains (only) the vortex v_j. If so, then the two vortices are mutual nearest neighbours of opposite sign, and are classified as a dipole (e.g. vortices v_1 and v_2 in figure 3). If not, then the vortices are left unclassified (e.g. vortices v_6 and v_5 in figure 3).

(ii) *Clusters:* If a list $\boldsymbol{l}_j$ consists of a set of cluster candidate vortices $\{v_k\}$, then the lists $\{\boldsymbol{l}_k\}$ are all checked to see if they contain the vortex v_j. For each list $\boldsymbol{l}_k$ that does contain v_j, the two vortices v_j and v_k are labelled as belonging to the same cluster (e.g. in figure 3, vortex v_4 'checks' both $\boldsymbol{l}_3$ and $\boldsymbol{l}_5$ to see if it is a member of either. It is found to be a member of both, so all three vortices are placed in a single cluster). For each list $\boldsymbol{l}_k$ that does not contain v_j, neither vortex label is updated (e.g. vortex v_7 and v_{10} in figure 3). Note that not all members of a single cluster have to be mutual candidates of one another. In the example shown in figure 3,

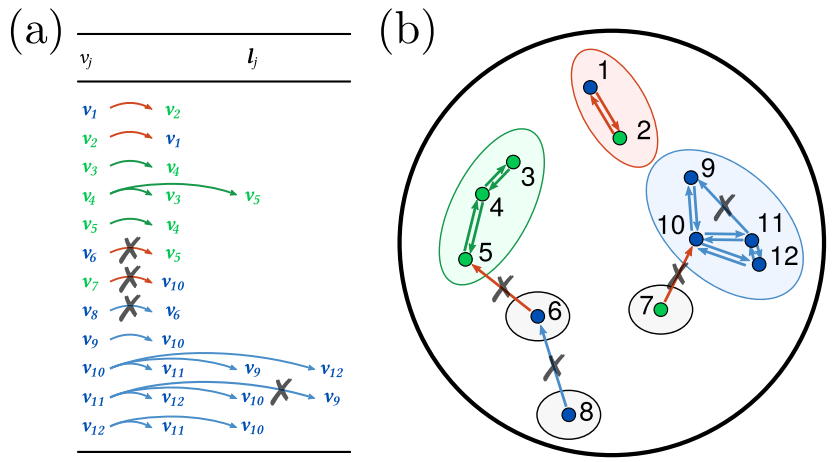

Figure 3. The process of identifying mutual neighbours, shown equivalently as (a) a table of candidate lists $\boldsymbol{l}_j$ taken from table 1, and (b) drawn directly onto the example vortex configuration from figure 2. An arrow is drawn from each vortex v_j to all the members of its candidate list $\boldsymbol{l}_j$. Only when arrows point in both directions between v_j and v_k are they defined to be mutual neighbours. All arrows that are one-directional have been crossed out in both panels. In panel (b), shaded ovals are drawn around clusters (blue/green for positive/negative), dipoles (red) and free vortices (black).

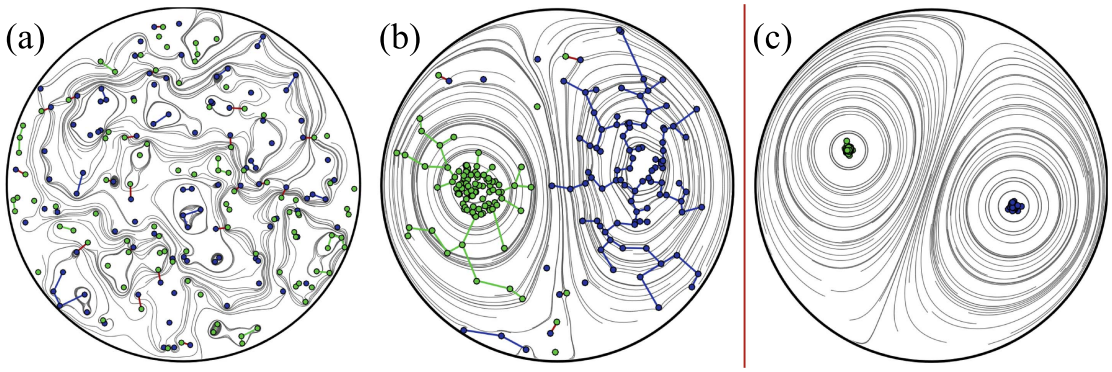

Figure 4. Representative neutral vortex configurations (a)–(c) at respective temperatures $T/T_{\mathrm{EBC}} = 10^6$, 1.022, and 0.778, with $T_{\mathrm{EBC}} = -0.25\alpha N_{\mathrm{tot}}$ and $N_{\mathrm{tot}} = 200$. Vortices in vortex and antivortex clusters are connected by blue and green lines, respectively, vortex and an antivortex in vortex dipoles are connected by red lines and free vortices are marked by isolated filled circles. The streamlines illustrate the velocity field generated by the collection of vortices. The red vertical line indicates the location of the condensation transition point T_{EBC} between (b) and (c).

v_9 is only a mutual neighbour with v_{10}, but is still placed in the same cluster as v_{11} and v_{12}. As the algorithm proceeds, vortices may be assigned to existing clusters, or previously classified clusters may become merged.

Any vortices left unclassified after this process are classified as free vortices, as they have no mutual dipole or cluster neighbours (e.g. vortex v_6 in figure 3).

In figure 3(b), any two vortices that are connected by a two-directional link are part of the same cluster or dipole, while any vortex that has no two-directional links is a free vortex.

To reduce computation, the checking of mutual candidates can be restricted such that it is only initiated for v_j and v_k if $j > k$. Alternatively, once a pair of vortices has been checked, then v_j could be removed from $\boldsymbol{l}_k$ and vice versa.

7. Two vortex species results

To study the thermodynamics of the condensation of Onsager vortices, we have performed Monte Carlo calculations using a Metropolis algorithm to find the equilibrium vortex configurations as functions of temperature for systems with 10, 20, 50, 100, 200, 300 and 400 vortices [12, 13]. The Monte Carlo calculations, and the conclusions drawn from the results, are obtained using canonical ensemble with hard core vortex core regularisation. A hard core diameter of $2\xi = 0.001\, R_\circ$ was imposed on each vortex in the results presented. The Monte Carlo samplings were performed for temperature in the range $T \in (-\infty, -0)$ with 10^6 microstates at

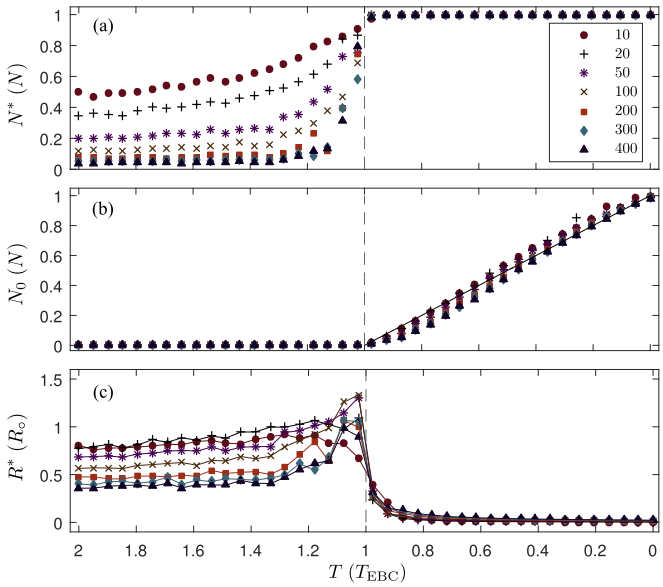

Figure 5. Fraction of vortices in the largest cluster (a), the condensate fraction, equation (13), (b) and the mean cluster radius $R^* = 4\mathrm{Std}(r_j)$, where $\mathbf{r}_j$ is the vector of positions of the vortices in the largest cluster (c) as functions of scaled temperature. Data is shown for systems with different vortex numbers as indicated in the legend. The function $1 - \mathrm{T}/T_{\rm EBC}$, where $T_{\rm EBC} = -0.25\alpha N_{\rm tot}$, is shown as a solid line in (b) for $|T| < |T_{\rm EBC}|$ and the vertical dashed line marks the critical point. All quantities are ensemble averaged. The few percent standard statistical uncertainty in the data, $1/\sqrt{1000}$, yields a reasonable estimate outside the fluctuation region despite being a lower bound due to the inherent correlations of the Markov chain Monte Carlo method employed.

each temperature after initial burn in of 10^6 steps. Out of the 10^6 microstates, 1000 uniformly spaced configurations were recorded and used for vortex classification analysis.

Figure 4 shows typical vortex configurations of disordered and strongly clustered neutral vortex states of $N_{\rm tot} = 200$ vortices obtained from the Monte Carlo calculations at different temperatures. The same sign clusters, dipoles and free vortices are identified using the vortex classification algorithm and the velocity field stream lines are included to visualise the superflow around the vortices. Figure 4(a) shows a vortex configuration at a high negative temperature $T = 10^6\ T_{\rm EBC}$ revealing a fairly disordered configuration of vortices with an abundance of vortex dipoles and small clusters. Figure 4(b) shows a vortex configuration at $T = 1.022\ T_{\rm EBC}$ close to the critical temperature. In figure 4(b) nearly all the vortices have already clustered into two large Onsager vortices although the condensate fraction remains zero. Figure 4(c) shows Onsager vortices at temperature $T = 0.778\ T_{\rm EBC}$ where the system has a condensate fraction of $N_0/N \approx 0.1$. The prominent dipolar shape of the streamlines in (b) and (c) is a by product that emerges enroute to condensation of the Onsager vortices and is observable before the critical point $T = T_{\rm EBC}$, indicated by the red vertical line, see also supplemental figure S1(b) of [13].

Figure 5 shows (a) the largest cluster fraction, (b) the condensate fraction, and (c) the mean radius of the largest cluster in the system as functions of temperature in units of the critical temperature $T_{\rm EBC} = -0.25\alpha N_{\rm tot}$. The largest cluster fraction figure 5(a) is strongly dependent on the total number of vortices in the system. In contrast, the condensate fraction, shown in figure 5(b), remains zero at all temperatures $|T| > |T_{\rm EBC}|$ and thereafter increases as the absolute negative zero is approached. Figure 5(c) shows the mean radii of the largest vortex clusters as functions of temperature. As the critical temperature is approached from the disordered side, the largest cluster tends to grow in size as ever more vortices are joining the cluster. In the condensed phase the cluster rapidly shrinks as the phase-space density, and hence the condensate fraction, increases. Importantly, the condensate fraction shows universality in the sense that it is consistent with data collapsing onto a single curve, indicating the condensate fraction becoming a vortex number independent quantity in the large vortex number limit.

With the ability to quantify the condensation of Onsager vortices, we have revisited the dynamical mean-field simulations of [34]. Figure 6 shows a typical result revealing that in this neutral vortex system, the largest cluster fraction and vortex dipole moment are practically equivalent observables. However, although the system is continually evaporatively heated, the condensate fraction remains zero for all times. The initial vortex number in this simulation is 100 and it decays to the final value of 12. Comparing the largest cluster fraction in figure 6 with 5(a) shows that this system is initially at temperature $|T| \gg |T_{\rm EBC}|$ and evaporatively heats reaching a final temperature of $|T| \gtrsim |T_{\rm EBC}|$. Quantitatively, the temperature of the vortex system can be found using the vortex thermometry based on the fraction of clustered vortices in the system [45]. However, once the system becomes fully clustered, the evaporative heating mechanism switches off [13] and the condensation is unable to proceed.

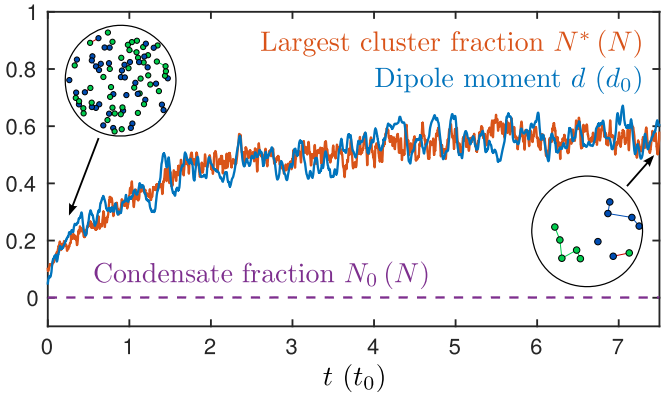

Figure 6. Dipole moment of the vortex configuration (solid blue) expressed in units of $d_0 = \kappa R_s N$, largest cluster fraction (solid orange) and condensate fraction (dashed purple) as functions of time calculated from a dynamical mean-field simulation. The unit of time is $t_0 = \hbar/\mu_{\rm GPE}$, where $\mu_{\rm GPE}$ is the chemical potential of the Gross–Pitaevskii equation. The initial vortex number is 100 and as the system evaporatively heats up, the vortex number decays to a value of 12 at the end of the simulation, see [34] for details.

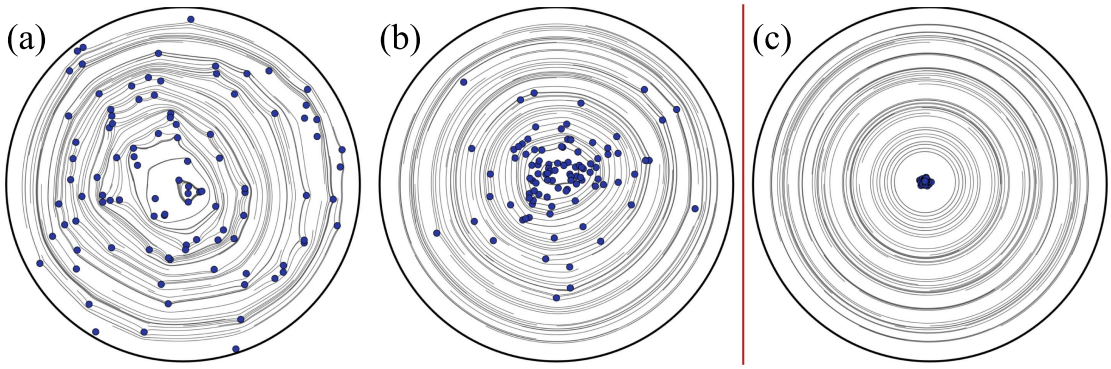

Figure 7. Representative charge-polarised vortex configurations (a)–(c) at respective temperatures $T/T_{\rm EBC} = 2.000$, 1.031, and 0.769, with $T_{\rm EBC} = -0.5\alpha N_v$ and $N_v = 100$. The streamlines illustrate the velocity field generated by the collection of vortices. The red vertical line indicates the location of the condensation transition point between (b) and (c).

8. One vortex species results

Clustering of vortices and their condensation are two separate phenomena. Vortex clusters exist at all negative temperatures [45], where as non-zero condensate fraction only exists in the temperature range $0 > T > T_{\rm EBC}$. To demonstrate this more clearly, we have performed Monte Carlo calculations for a charge-polarised, $\sum_{i=1}^{N_v} s_i = N_v$, case where only one species of vortices is present in the system. Figures 7(a)–(c) shows the vortex configurations at three different temperatures. These vortex configurations illustrate the fact that the vortex positions suddenly collapse when the radius of the host Onsager vortex cluster drops below a critical value, R_c. The transition illustrated in figure 4 corresponds to independent condensation of two-species of vortices at the same temperature due to the equal numbers of vortices and antivortices. In vortex number imbalanced systems there are two, vortex number dependent, critical temperatures $T_{\rm maj} = -\alpha N_{\rm maj}/2$ and $T_{\rm min} \approx -\alpha N_{\rm min}/2$.

The critical temperature for the condensation of an Onsager vortex in a single vortex species system may be predicted by a similar free energy argument as for two vortex species systems [11, 13]. The Helmholtz free energy, $F = E - TS$, of a vortex configuration where all N_v vortices are concentrated inside a circular region of radius R^* is

$$F \approx \frac{\rho_s \kappa^2}{4\pi} N_v^2 \ln\left(\frac{R}{R^*}\right) - Tk_{\rm B} \ln\left(\frac{R^*}{R}\right)^{2N_v}, \tag{14}$$

where the energy E is that of a multiply quantised vortex of core radius R^* and the entropy S is obtained as the logarithm of a statistical weight of the configuration. A change in the sign of the free energy signifies that the probability $p_F \propto {\rm e}^{-F/k_{\rm B}T}$ of observing such a configuration becomes exceedingly likely and predicts a critical temperature

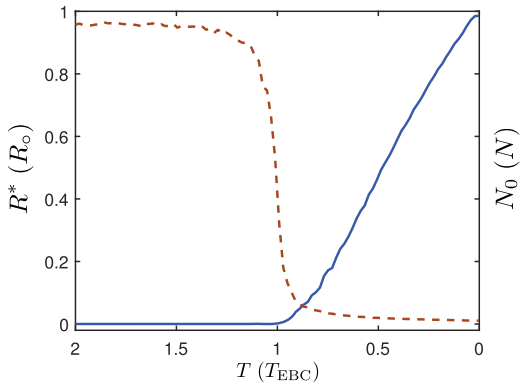

Figure 8. Condensate fraction of $N_v = 100$ single species, $s = +1$, vortices as a function of temperature (right axis, solid line) and the radius, R^*, of the vortex cluster, (left axis, dashed line), as a function of reduced temperature.

$$T_{\rm EBC} = -\frac{\alpha N_v}{2} = -\frac{\alpha N_{\rm tot}}{4}, \tag{15}$$

which is the same for a single species system with N_v vortices as it is for a two-species system with the same number, $N_v = N_{\rm tot}/2$, of vortices of one species.

In the general imbalanced case with N_+ vortices and N_-antivortices with $N_{\rm tot} = N_+ + N_- = N_{\rm maj} + N_{\rm min}$ and $N_{\rm maj} > N_{\rm min}$ there are two critical temperatures corresponding to separate condensation of each of the two vortex species. When the temperature approaches negative zero, the majority species condenses first at $T_{\rm maj} = -\alpha N_{\rm maj}/2$, followed by the condensation of the minority species at $T_{\rm min} \approx -\alpha N_{\rm min}/2$, where the latter is shifted slightly toward negative zero due to the interaction with the condensate of the majority species.

The condensation of Onsager vortices may be viewed from the point of view of competition between solid body rotation within the core of the vortex cluster and potential flow outside the cluster, see equations (7) and (8). Balancing the kinetic energy contributions of these two velocity fields in the mean-field interaction energy term in equation (11) predicts a critical cluster radius

$$R_{\rm c} = {\rm e}^{-1/4} R_\circ \approx 0.778800 R_\circ, \tag{16}$$

such that for $T/T_{\rm EBC} > 1$ the whole system prefers to mimic solid body rotation of a classical fluid, figures 7(a) and (b), whereas for $T/T_{\rm EBC} < 1$ the system prefers to mimic the velocity field of a quantised superfluid vortex, figure 7(c).

Figure 8 shows the condensate fraction measured using equation (13). For $T/T_{\rm EBC} > 1$, vortices are found scattered everywhere within the circular boundary and the condensate fraction is strictly zero. Near the transition, the vortices begin to clump and at critical radius $R_{\rm c}$ the vortex cluster suddenly begins to collapse. Accompanied with the shrinking of the vortex cluster, the condensate fraction grows almost linearly with the reduced temperature.

According to equation (14) the specific heat at the transition

$$c_v = N_v^2 \frac{\rho_s \kappa^2}{4\pi} \frac{1}{R^*} \frac{\partial R^*(T)}{\partial T}\bigg|_{T_{\rm EBC}} \propto (T - T_{\rm EBC})^{-1}, \tag{17}$$

where in the last step we have assumed linear dependence of the cluster radius on the temperature in the vicinity of the transition, as suggested by figure 8.

Figure 9(a) shows the phase space density, $n_v \langle \lambda_v \rangle$ of the vortices as functions of position and reduced temperature. The 1D vortex–particle density $n(x)$ is obtained by modelling each vortex–particle by a normalised Gaussian wave packet of waist λ_v. The frames (b)–(d) show the 1D density $n(x)$ of the vortex gas for three different temperatures $T/T_{\rm EBC} = 2, 1.031$, and 0.769. For $T/T_{\rm EBC} > 1$ the vortex density is spread over the whole system while below the transition the vortex density becomes localised both in real space and in vortex momentum space.

On approaching the condensation transition from the infinite temperature side the asymptotic form of the 2D real space vortex density is predicted to be [56, 57]

$$\rho_v(r) = \frac{1}{\pi}\left[\left(1 - \frac{T_{\rm EBC}}{T}\right)\left(1 + \frac{T_{\rm EBC}}{T - T_{\rm EBC}} r^2\right)^2\right]^{-1} \tag{18}$$

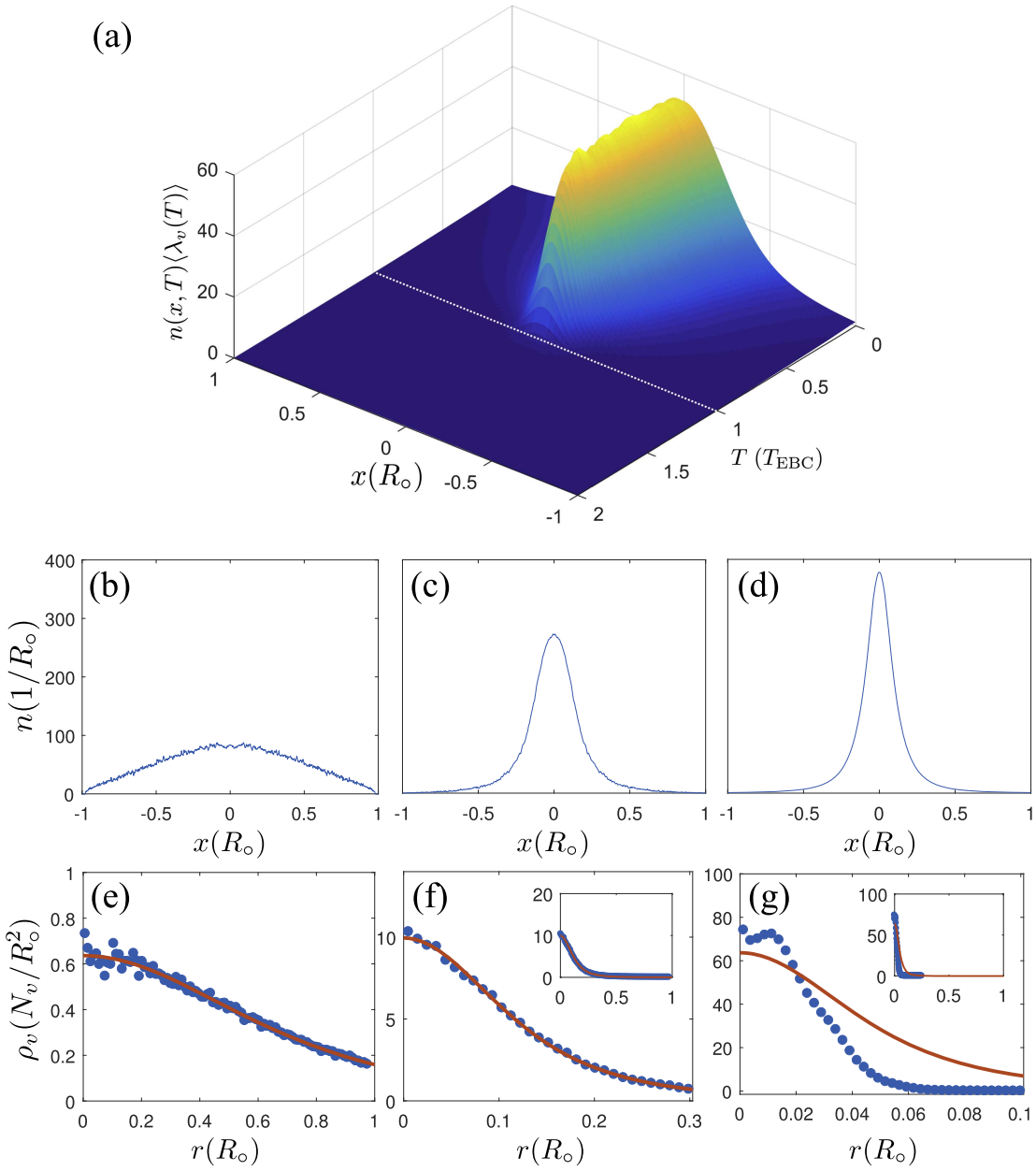

Figure 9. Phase-space density (a) as functions of position and reduced temperature, 1D vortex–particle densities (b)–(d) as functions of position corresponding to the representative charge-polarised vortex configurations at respective temperatures $T/T_{\rm EBC} = 2.000, 1.031$, and 0.769, for $N_v = 100$ with $T_{\rm EBC} = -0.5\alpha N_v$, and (e)–(g) the 2D density of the vortices in real space as functions of radial distance from the centre of the disc at temperatures corresponding to (b)–(d). The orange solid lines in (e)–(g) are least squares fits to theoretical vortex density function in equation (18) with $T_{\rm fit}/T_{\rm EBC} = 2.004, 1.033$, and (1.005).

for $T/T_{\rm EBC} > 1$, with normalisation

$$2\pi \int_0^{R_\circ} \rho_v(r) r dr = N_v. \tag{19}$$

Figures 9(e)–(g) shows the least squares fits of the function (18) to the radial 2D real space vortex density measured from the Monte Carlo calculations. Using the temperature T as the sole fitting parameter the best fitting temperatures are measured to be $T_{\rm fit}/T_{\rm EBC} = 2.004, 1.033$, and (1.005) and the resulting density profiles predicted by equation (18) are shown as orange curves. The parentheses are used here to denote that equation (18) is used in a regime outside its validity. While the theory prediction, equation (18), for the radial 2D vortex densities is in excellent agreement with the Monte Carlo data shown in figures 9(e) and (f), the theory curve in figure 9(g) is clearly unphysical because the prediction of equation (18) diverges at $T = T_{\rm EBC}$ and cannot be used for modelling the vortex density in the condensed phase for which $T/T_{\rm EBC} < 1$. This is evident in figure 9(g) where the best fitting function has $T_{\rm fit}/T_{\rm EBC} = (1.005)$, as opposed to the actual temperature $T/T_{\rm EBC} = 0.769$, of the state.

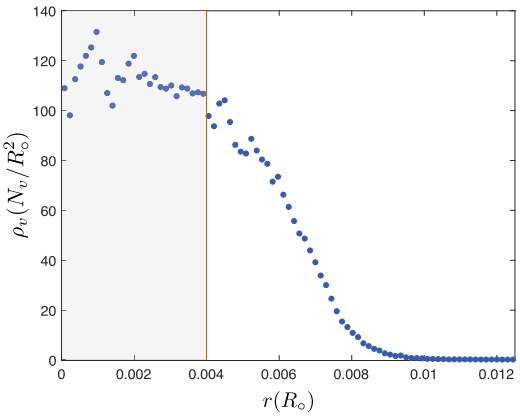

Figure 10. Two-dimensional vortex density in real space as a function of radial distance measured from the centre-of-mass of the vortex cluster. The temperature, condensate fraction and condensate radius of this state are, respectively, $T/T_{\rm EBC} = 0.244$, $N_0/N = 0.773$, and $R_{\rm cond}/R_\circ = 0.004$. The condensate corresponds to the shaded area with flat, incompressible, density of the vortex fluid.

Figure 10 shows the 2D vortex density as a function of radial position for $T/T_{\rm EBC} = 0.244$. The condensed vortices within the cluster seem to form a fluid like incompressible core with a constant vortex density. The number of vortices within the shaded region corresponds to the condensate and is equal to N_0.

9. Discussion

The physics of the vortex system in the vicinity of the critical negative absolute temperature

$$T_{\rm EBC} = -\frac{\hbar\omega_k}{2k_{\rm B}}\frac{m_0}{m}N_v = -\frac{\hbar\omega_k}{4k_{\rm B}}\frac{m_0}{m}N_{\rm tot}, \tag{20}$$

where ω_k is the kelvon frequency and m_0 is the vortex mass per unit length [53], has been discussed extensively in the recent literature [13, 34–43, 45, 58] yet the nature of the condensate has remained unclear. This is partly because of the divergent behaviour of the zero-core point vortex model that becomes invalid at the critical point of condensation and is unable to yield predictions for the condensed phase. The situation is the same as in the positive temperature side where the Hauge–Hemmer transition to pair-collapsed phase in the zero-core point vortex model is divergent and the structure of the vortex core, which is always present in any real physical system, must be accounted for. Including the effects of non-zero vortex cores in the positive temperature systems allows correct treatment of the BKT phase transition whose critical temperature is shifted by a factor of 2 with respect to the Hauge–Hemmer transition that occurs at $T_{\rm HH} = \alpha$ [15]. Similarly, any self-consistent treatment of the negative absolute temperature Onsager vortex condensate must include the effects of non-zero size of the vortex core. For the sake of clarity, we discuss the one and two vortex species cases separately below.

9.1. One vortex species case

Considering the single vortex species system shows that the condensation of the Onsager vortices occurs when the vortex cores within a cluster of vortices begin to merge into a single vortex structure with multiple circulation quanta, signifying the emergence of large degeneracy in the quasiparticle degrees of freedom of the vortices.

We briefly recall the underpinnings of the quantum Hall effect of 2D electron gas in a strong external magnetic field corresponding to extremely large kinetic energy per electron. This 2D problem is often theoretically mapped onto a dual 1D harmonic oscillator problem, which reveals that the topological phase transitions to the integer quantum Hall states occur when the electrons condense in the highly degenerate lowest Landau level. Although the electrons move in 2D space, the topological phase transitions are quantified in terms of the eigenstates of a 1D harmonic oscillator.

Similar physics is pertinent to the Onsager vortex condensation transition. It is therefore useful to consider the closest known physical realisation of the Onsager's point vortex model, which is a Bose–Einstein condensate with quantised vortices nucleated in the macroscopic condensate wavefunction. A trial wave function for such a system may be expressed as

$$\Psi(\mathbf{r}) = \prod_{j=1}^{N_v} \chi_1(r_j)\sqrt{f}\,{\rm e}^{{\rm i}\theta_j}, \tag{21}$$

where $r_j = \sqrt{(x - x_j)^2 + (y - y_j)^2}$ and f is the smooth condensate particle density in the absence of the vortices, $\theta_j = \arg[(x - x_j) + \mathrm{i}(y - y_j)]$ are the additive phase functions with singularities at the vortex locations $\{x_j, y_j\}$, and the (soft) vortex core function

$$\chi_1(r_j) = \frac{r_j}{\sqrt{r_j^2 + 2\xi^2}}. \tag{22}$$

The probability current

$$\mathbf{j} = \frac{\hbar}{2m\mathrm{i}}[\Psi(\mathbf{r})^*\nabla\Psi(\mathbf{r}) - \Psi(\mathbf{r})\nabla\Psi^*(\mathbf{r})] \equiv |\Psi(\mathbf{r})|^2\mathbf{v}_s \tag{23}$$

of the state (21) defines the superfluid velocity field $\mathbf{v}_s$, the incompressible component of which is remarkably well approximated by the velocity field of Onsager's point vortex model [59].

The elementary excitation spectrum of a 2D vortex configuration is obtained by solving the Bogoliubov–de Gennes (BdG) eigenvalue problem [60]. The N_v phase singularities due to the N_v quantised vortices in the system yield N_v low energy quasiparticle eigenstates [61] that satisfy the bosonic commutation relations

$$[\eta_q, \eta_p^\dagger] = \delta_{q,p}; \qquad [\eta_q, \eta_p] = [\eta_q^\dagger, \eta_p^\dagger] = 0, \tag{24}$$

where $\eta_q^\dagger$ and η_q are the usual Bogoliubov quasiparticle creation and annihilation operators. In accordance with the quasiparticle picture of superfluids, the macroscopic multiply connected wave function, equation (21), may be expressed in terms of the countably infinite set of such quasiparticle states [60]. These Bogoliubov quasiparticles are bosons and this property is inherited by the host vortices whose circulation is quantised.

For a single vortex with N_v circulation quanta the condensate wave function may be expressed as

$$\Psi(\mathbf{r}) = \chi_{N_v}(r)\sqrt{f}\mathrm{e}^{\mathrm{i}N_v\theta}, \tag{25}$$

with

$$\chi_{N_v}(r) = \frac{r}{\sqrt{r^2 + 2N_v\xi^2}} \tag{26}$$

is the structure function of the vortex core with N_v circulation quanta. The BdG quasiparticle excitation spectrum of such a state has only one vortex eigenmode, corresponding to the one phase singularity, with orbital angular momentum quantum number equal to $\ell = -N_v$ [62]. This high-winding number bosonic quasiparticle mode is a BEC of N_v Bogoliubov quasiparticles associated with the N_v vortex circulation quanta, in essence forming a 'vortex BEC in a BEC of atoms'. Such quasiparticle condensates are not unusual. For example, magnons (spin-waves) have previously been observed to form Bose–Einstein condensates of their own within their host BECs [63–65].

The circulation

$$\Gamma = \oint_C \mathbf{v}\cdot\mathrm{d}\boldsymbol{\ell} \tag{27}$$

of a classical point vortex measured along a path C that encloses the vortex is invariant with respect to continuous deformations of the path C precisely as for a quantised vortex in a BEC of atoms. In a BEC of atoms the vortex cores trap the bosonic quasiparticles (kelvons) and when these localised bosonic modes overlap they may form a condensate. The vortex density of the point-like vortex cores thus effectively measures the density of states of the Bogoliubov quasiparticles attached to the vortices and the overlapping of the vortex cores is tantamount to the condensation of the N_v BdG quasiparticles associated with the vortex degrees of freedom. It is in this sense that the classical point vortex Hamiltonian describes the bosonic degrees of freedom of the quantised vortices and their quantum statistical condensation at T_{EBC}. Indeed, equation (14) applies equally well for both classical point vortices and for quantised vortices in a BEC.

The vortex–particle duality allows a 1D treatment of the 2D vortex gas and motivates the definition of the vortex condensate fraction as

$$\frac{N_0}{N} = \frac{\xi^2}{\langle r_{\mathrm{nn}}\rangle^2}. \tag{28}$$

The condensate fraction is equal to the area ratio of the minimum possible phase-space area occupied by the N_v vortices to the area actually occupied by them. A high vortex condensate fraction is equivalent to strong overlap between the BdG quasiparticle modes of the quantised vortices. The point vortex model description works well in this extreme states of vortices because in such situations kinetic energy of the BEC of atoms is overwhelmingly larger than the usual mean-field atom–atom interaction.

It is interesting to recall the structure of a simple vortex in a superfluid or a superconductor. Outside the vortex core the superfluid or superconducting order parameter is at its bulk value whereas in the vortex core region the superfluid order parameter vanishes and the original symmetry of the full Hamiltonian is locally

restored. A local observer spatially traversing across a vortex core in such systems measures superfluid-normal-superfluid phase changes along their path.

For a two vortex problem, the change in the phase space topology of the point vortex model has been quantified by identification of the phase-space wall that divides the two regions of phase space where the vortex trajectories are either overlapping or non-overlapping [66]. We conjecture that similar phase-space dividing walls are associated with any number N_v of vortices and that associated with the condensation of Onsager vortices a multiply connected phase-space topology transforms to a single connected region. In this sense, the condensation of Onsager vortices could be viewed as a topological phase transition.

9.2. Two vortex species case

In the neutral two vortex species case, the Onsager vortex condensation transition described above for single vortex species systems occurs in both of the vortex types separately, and simultaneously. In the case of vortex-imbalanced system the majority vortex species condenses first at

$$T_{\rm maj} = -\alpha N_{\rm maj}/2, \tag{29}$$

followed by the condensation of the minority species at

$$T_{\rm min} \approx -\alpha N_{\rm min}/2, \tag{30}$$

where $T_{\rm min}$ shifted slightly toward negative zero due to the interaction with the condensate of the majority species.

Before the condensation of the Onsager vortices proceeds, the vortices become spatially phase separated as shown e.g. in figure 4 and in the supplemental figure S1(b) of [13]. Such phase separation is one step in the sequence of phase space compactification leading to the EBC transition. Hence, the apparent symmetry breaking associated with the spatial separation of the centres of mass of the two vortex species is a by product that emerges enroute to the Einstein–Bose condensation of the Onsager vortices. The critical temperature is the same for a single species system with N_v vortices as it is for a two-species system with the same number, $N_v = N_{\rm tot}/2$, of vortices of one species, and the condensation transition occurs in both systems. In contrast, the phase separation is specific to the two-species case.

10. Conclusions

In conclusion, we have employed a vortex–particle duality to establish a correspondence between vortices in a 2D fluid and a 1D gas of vortex particles. Using this mapping, we have provided a quantitative measure for the condensation of Onsager vortices—a vortex condensate fraction. The vortex condensate forms due to the overlap of the vortex cores. Ultimately, deep in the condensed phase a phase-space Wigner crystallisation of vortices with hard cores takes place [13] while soft core vortices should yield multiple quantum vortex state [62]. The situation bears resemblance to rapidly rotating neutral superfluids that are predicted to undergo phase changes when the vortex cores begin to significantly overlap and the filling factor, or the number of fluid particles per vortex, approaches unity [67, 68]. One interesting future direction would indeed be to consider a quantised form of the 1D vortex Hamiltonian and to study the potentially emerging fractional quantum Hall-like states in the Onsager vortex condensates. Another direction would be to study connections between the 1D vortex particle theory and other 1D systems [55, 69, 70].

The first observations of negative absolute temperatures and Onsager vortices in neutral vortex gas, where absolute negative temperature states are readily associated with the emergence of conspicuous vortex clusters, has recently been reported in two landmark experiments [7, 8]. The most extreme negative temperature states realised so far were estimated to correspond to a vortex temperature of $T = 1.14\, T_{\rm EBC}$ and a condensate fraction $N_0/N \approx 18/57^2$ [7]. Since the largest cluster in these experiments had on average 9 vortices, and if the minimum size of a condensate should be 2 vortices, the critical temperature $T_{\rm EBC}$ in such a system would, due to a finite size effect, correspond to a condensate fraction of 2/9. This means that to observe the condensation of Onsager vortices, even higher vortex energy states are required.

It seems that the most suitable system to study the critical physics of Einstein–Bose condensation of Onsager vortices is a single species vortex system. We therefore propose an experiment to observe condensates of Onsager vortices using a BEC or superfluid Fermi gas of atoms by creating a giant vortex with multiple circulation quanta using, e.g., topological phase imprinting [71] or high-winding number Laguerre–Gauss laser beams [72], to imprint a multiply quantised, $N_v \gg 2$, quantum vortex into a superfluid in a preferably uniform trap [7, 8, 26–33]. Subsequently monitoring the slow decay of the state into N_v singly quantised vortices, evolving from configurations akin to figure 7(c) to those shown in (b), will enable quantitative observation of crossing the critical temperature $T_{\rm EBC}$. The vortex decay may be initiated by dynamical instabilities [73–75] with the subsequent quantum turbulent ergodic dynamics allowing the vortices to equilibrate to a well defined vortex

temperature [45]. Hence, starting from a 100% EBC, the vortices are anticipated to slowly evaporate from the condensate, ultimately leaving only a quantum turbulent thermal cloud of single quantum vortices in the system. An additional benefit of this approach is that it does not require detection of the vortex circulation signs [8, 25, 76]. Direct measurement of the vortex positions and their core sizes enables direct measurement of the condensate fraction N_0/N, equation (28), in the condensed phase for $T/T_{\rm EBC} < 1$. Equation (18) enables explicit and accurate measurement of the vortex temperature for $T/T_{\rm EBC} > 1$, as shown in figures 9(e) and (f). In combination, these two measurements will enable direct and quantitative experimental observation of the condensation transition of the Onsager vortices.

Acknowledgments

We acknowledge support from an Australian Postgraduate Award (RN, AG), the Australian Research Council via Discovery Project No. DP130102321 and DP170104180 (TS), and the nVidia Hardware Grant Program. This research was undertaken with the assistance of resources from the National Computational Infrastructure (NCI), which is supported by the Australian Government.

ORCID iDs

Tapio P Simula https://orcid.org/0000-0003-0730-9126

References

[1] Onsager L 1949 *Il Nuovo Cimento Ser.* 9 **6** 279–87
[2] Eyink G L and Sreenivasan K R 2006 *Rev. Mod. Phys.* **78** 87–135
[3] Purcell E M and Pound R V 1951 *Phys. Rev.* **81** 279–80
[4] Oja A S and Lounasmaa O V 1997 *Rev. Mod. Phys.* **69** 1–136
[5] Abraham E and Penrose O 2017 *Phys. Rev.* E **95** 012125
[6] Braun S, Ronzheimer J P, Schreiber M, Hodgman S S, Rom T, Bloch I and Schneider U 2013 *Science* **339** 52–5
[7] Gauthier G, Reeves M T, Yu X, Bradley A S, Baker M, Bell T A, Rubinsztein-Dunlop H, Davis M J and Neely T W 2018 arXiv:1801.06951
[8] Johnstone S P, Groszek A J, Starkey P T, Billington C J, Simula T P and Helmerson K 2018 arXiv:1801.06952
[9] Kraichnan R H 1967 *Phys. Fluids* **10** 1417–23
[10] Kraichnan R H 1975 *J. Fluid Mech.* **67** 155–75
[11] Kraichnan R H and Montgomery D 1980 *Rep. Prog. Phys.* **43** 547–619
[12] Viecelli J A 1995 *Phys. Fluids* **7** 1402–17
[13] Simula T, Davis M J and Helmerson K 2014 *Phys. Rev. Lett.* **113** 165302
[14] Salzberg A M and Prager S 1963 *J. Chem. Phys.* **38** 2587
[15] Hauge E H and Hemmer P C 1971 *Phys. Norv.* **5** 209
[16] Berezinskii V L 1971 *Sov. Phys.—JETP* **32** 493
[17] Berezinskii V L 1972 *Sov. Phys.—JETP* **34** 610
[18] Kosterlitz J M and Thouless D J 1973 *J. Phys. C: Solid State Phys.* **6** 1181
[19] Neely T W, Samson E C, Bradley A S, Davis M J and Anderson B P 2010 *Phys. Rev. Lett.* **104** 160401
[20] Navarro R, Carretero-González R, Torres P J, Kevrekidis P G, Frantzeskakis D J, Ray M W, Altuntaş E and Hall D S 2013 *Phys. Rev. Lett.* **110** 225301
[21] Henn E A L, Seman J A, Roati G, Magalhães K M F and Bagnato V S 2009 *Phys. Rev. Lett.* **103** 045301
[22] Neely T W, Bradley A S, Samson E C, Rooney S J, Wright E M, Law K J H, Carretero-González R, Kevrekidis P G, Davis M J and Anderson B P 2013 *Phys. Rev. Lett.* **111** 235301
[23] Kwon W J, Moon G, Choi J Y, Seo S W and Shin Y I 2014 *Phys. Rev.* A **90** 063627
[24] Kwon W J, Kim J H, Seo S W and Shin Y I 2016 Observation of von Kármán vortex street in an atomic superfluid gas *Phys. Rev. Lett.* **117** 245301
[25] Seo S W, Ko B, Kim J H and Shin Y 2017 *Sci. Rep.* **7** 4587
[26] Henderson K, Ryu C, MacCormick C and Boshier M G 2009 *New J. Phys.* **11** 043030
[27] Gaunt A L, Schmidutz T F, Gotlibovych I, Smith R P and Hadzibabic Z 2013 *Phys. Rev. Lett.* **110** 200406
[28] Chomaz L, Corman L, Bienaimé T, Desbuquois R, Weitenberg C, Nascimbène S, Beugnon J and Dalibard J 2015 *Nat. Commun.* **6** 6162
[29] Bell T A, Glidden J A P, Humbert L, Bromley M W J, Haine S A, Davis M J, Neely T W, Baker M A and Rubinsztein-Dunlop H 2016 *New J. Phys.* **18** 035003
[30] Eckel S, Lee J G, Jendrzejewski F, Lobb C J, Campbell G K and Hill W T 2016 *Phys. Rev.* A **93** 063619
[31] Gauthier G, Lenton I, Parry N M, Baker M, Davis M J, Rubinsztein-Dunlop H and Neely T W 2016 *Optica* **3** 1136–43
[32] Mukherjee B, Yan Z, Patel P B, Hadzibabic Z, Yefsah T, Struck J and Zwierlein M W 2017 *Phys. Rev. Lett.* **118** 123401
[33] Hueck K, Luick N, Sobirey L, Siegl J, Lompe T and Moritz H 2018 *Phys. Rev. Lett.* **120** 060402
[34] Groszek A J, Simula T P, Paganin D M and Helmerson K 2016 *Phys. Rev.* A **93** 043614
[35] Stagg G W, Allen A J, Parker N G and Barenghi C F 2015 *Phys. Rev.* A **91** 013612
[36] White A C, Barenghi C F and Proukakis N P 2012 *Phys. Rev.* A **86** 013635
[37] Reeves M T, Billam T P, Anderson B P and Bradley A S 2013 *Phys. Rev. Lett.* **110** 104501
[38] Billam T P, Reeves M T, Anderson B P and Bradley A S 2014 *Phys. Rev. Lett.* **112** 145301
[39] Reeves M T, Billam T P, Anderson B P and Bradley A S 2015 *Phys. Rev. Lett.* **114** 155302
[40] Skaugen A and Angheluta L 2016 *Phys. Rev.* E **93** 032106
[41] Yu X, Billam T P, Nian J, Reeves M T and Bradley A S 2016 *Phys. Rev.* A **94** 023602

[42] Skaugen A and Angheluta L 2017 *Phys. Rev.* E **95** 052144
[43] Salman H and Maestrini D 2016 *Phys. Rev.* A **94** 043642
[44] Yu X and Bradley A S 2017 *Phys. Rev. Lett.* **119** 185301
[45] Groszek A J, Davis M J, Paganin D M, Helmerson K and Simula T P 2018 *Phys. Rev. Lett.* **120** 034504
[46] Yatsuyanagi Y, Kiwamoto Y, Tomita H, Sano M M, Yoshida T and Ebisuzaki T 2005 *Phys. Rev. Lett.* **94** 054502
[47] Valani R N, Groszek A J and Simula T P 2016 arXiv:1612.02930
[48] Kagan Y, Kashurnikov V A, Krasavin A V, Prokof'ev N V and Svistunov B V 2000 *Phys. Rev.* A **61** 043608
[49] Hadzibabic Z, Krüger P, Cheneau M, Battelier B and Dalibard J 2006 *Nature* **441** 1118–21
[50] Cladé P, Ryu C, Ramanathan A, Helmerson K and Phillips W D 2009 *Phys. Rev. Lett.* **102** 170401
[51] Hung C L, Zhang X, Gemelke N and Chin C 2011 *Nature* **470** 236–9
[52] Pointin Y B and Lundgren T S 1976 *Phys. Fluids* **19** 1459–70
[53] Simula T 2018 *Phys. Rev.* A **97** 023609
[54] Keller J B 1958 *Ann. Phys.* **4** 180–8
[55] Giamarchi T 2003 *Quantum Physics in One Dimension* (*International Series of Monographs on Physics*) (Oxford: Clarendon)
[56] Lundgren T S and Pointin Y B 1977 *J. Stat. Phys.* **17** 323–55
[57] O'Neil T M and Smith R A 1992 *Phys. Fluids* B **4** 2720–8
[58] Esler J G 2017 *J. Stat. Phys.* **169** 1045–65
[59] Groszek A J, Paganin D M, Helmerson K and Simula T P 2018 *Phys. Rev.* A **97** 023617
[60] Fetter A L 1972 *Ann. Phys.* **70** 67–101
[61] Simula T 2013 *Phys. Rev.* A **87** 023630
[62] Simula T P, Virtanen S M M and Salomaa M M 2002 *Phys. Rev.* A **65** 033614
[63] Volovik G E 2008 *J. Low Temp. Phys.* **153** 266–84
[64] Demokritov S O, Demidov V E, Dzyapko O, Melkov G A, Serga A A, Hillebrands B and Slavin A N 2006 *Nature* **443** 430–3
[65] Vainio O *et al* 2015 *Phys. Rev. Lett.* **114** 125304
[66] Murray A V, Groszek A J, Kuopanportti P and Simula T 2016 *Phys. Rev.* A **93** 033649
[67] Cooper N R 2008 *Adv. Phys.* **57** 539–616
[68] Fetter A L 2009 *Rev. Mod. Phys.* **81** 647–91
[69] Terças H, Solnyshkov D D and Malpuech G 2013 *Phys. Rev. Lett.* **110** 035303
[70] Terças H, Solnyshkov D D and Malpuech G 2014 *Phys. Rev. Lett.* **113** 036403
[71] Leanhardt A E, Görlitz A, Chikkatur A P, Kielpinski D, Shin Y, Pritchard D E and Ketterle W 2002 *Phys. Rev. Lett.* **89** 190403
[72] Andersen M F, Ryu C, Cladé P, Natarajan V, Vaziri A, Helmerson K and Phillips W D 2006 *Phys. Rev. Lett.* **97** 170406
[73] Pu H, Law C K, Eberly J H and Bigelow N P 1999 *Phys. Rev.* A **59** 1533–7
[74] Kuopanportti P, Lundh E, Huhtamäki J A M, Pietilä V and Möttönen M 2010 *Phys. Rev.* A **81** 023603
[75] Cidrim A, White A C, Allen A J, Bagnato V S and Barenghi C F 2017 *Phys. Rev.* A **96** 023617
[76] Powis A T, Sammut S J and Simula T P 2014 *Phys. Rev. Lett.* **113** 165303